Intermittent oxidation kinetics and metal/oxide interfacial undulation

Dongxiang Wu,[1,*] Xianhu Sun,[1,*] Judith C. Yang,[2] and Guangwen Zhou[1,†]

[1]*Department of Mechanical Engineering & Materials Science and Engineering Program, State University of New York, Binghamton, New York 13902, USA*

[2]*Department of Chemical and Petroleum Engineering, University of Pittsburgh, Pittsburgh, Pennsylvania 15261, USA and Center for Functional Nanomaterials, Brookhaven National Laboratory, Upton, New York 11973, USA*

(Received 22 April 2024; revised 2 July 2024; accepted 17 July 2024; published 1 August 2024)

The phenomenon of oxygen adsorption induced surface restructuring is widespread across various metal-oxygen systems, yet its impact on initiating bulk oxide formation remains largely unexplored. Through *in situ* atomic-resolution electron microscopy observations of surface oxidation of Cu(110) and $Cu_{85}Au_{15}$(110), we unveil intermittent oxide-film growth modulated by oxygen-induced surface restructuring. This modulation is evidenced by repeated pinning of the Cu_2O growth front at isolated Cu columns of the $c(6\times2)$-O reconstruction, owing to required long-range diffusion of Cu and O atoms to the Cu_2O growth front. We reveal that Cu vacancies, generated at the Cu_2O growth front, are injected into the Cu_2O/Cu interface, inducing hill and valley undulation of the Cu_2O film. In contrast, atomic vacancies produced during the $Cu_{85}Au_{15}$(110) oxidation preferentially migrate into interfaces between Au-rich and Au-poor regions in the bulk, resulting in a flat and adherent Cu_2O film. These findings demonstrate the critical role of oxygen-induced surface restructuring in modulating oxide film growth kinetics and the manipulability of the fate of injected vacancies by alloying, thereby offering insights applicable to a broader range of metal-oxygen systems for fine-tuning oxidation kinetics and enhancing oxide/metal interfacial adhesion.

DOI: 10.1103/PhysRevB.110.085402

I. INTRODUCTION

The chemical affinity of metals for oxygen is of paramount importance across various industries, including energy, environmental, chemical, pharmaceutical, and microelectronics. This affinity can lead to both detrimental effects, such as causing serious corrosion problems, and beneficial processes, such as the production of important chemicals in heterogeneous catalysis and fabrication of gate oxides for electronic devices. A precise knowledge of the oxidation process is required to understand the complex key processes of the chemical and physical interactions between metals and oxygen. Typically, surface oxidation progresses from oxygen adsorption induced surface restructuring to subsequent oxide nucleation, growth, and finally, the development of a continuous oxide layer [1–4]. While significant research has focused on identifying the atomic structure of oxygen-induced surface restructuring under ultrahigh-vacuum conditions, directly discerning the atomic processes guiding the transformation from a two-dimensional oxygen-chemisorbed layer to a continuous oxide layer upon cumulative oxygen uptake has not been achievable. This challenge primarily arises from experimental limitations in monitoring the spatiotemporal evolution of local atomic configurations on the surface in reactive gas and high-temperature environments.

The advent of environmental transmission electron microscopy (ETEM) has opened avenues to bridge this knowledge gap by enabling the atomic-scale resolution of reaction dynamics at gas-solid interfaces [2,5–10]. Leveraging *in situ* ETEM imaging, herein we unveil the atomic-level mechanism underlying the onset of the bulk oxide formation and intermittent oxide film growth kinetics during the oxidation of Cu. By introducing gaseous O_2 to the sample region and employing high spatiotemporal TEM imaging, we can monitor the fast dynamics of local atomic configurations at both the gas-solid and solid-solid interfaces simultaneously. Our results reveal intriguing phenomena such as the intermittent kinetics of the Cu_2O film growth and the injection of atomic vacancies into the Cu_2O/Cu interface, leading to the hill and valley undulation of the Cu_2O film. In contrast, we observe preferential injection of vacancies into the interfaces between Au-rich and Au-poor regions in the bulk during the oxidation of $Cu_{85}Au_{15}$(110), resulting in an atomically flat and adherent Cu_2O film. Our selection of Cu as a model system is driven by two key considerations. First, Cu surfaces exhibit a series of surface reconstructions triggered by cumulative O_2 adsorption, a phenomenon shared by many other metal-oxygen systems. However, the impact of O_2-induced restructuring on the initiation of bulk oxide phase formation remains unaddressed. Secondly, the Cu-O system, like most transition metals, holds substantial technological importance, particularly in Cu-based catalysts, where surface oxidation and oxide overlay formation can exert a profound influence on catalytic process and overall efficiency [11–15].

II. MATERIALS AND METHODS

Cu(100) *and* $Cu_{85}Au_{15}$(100) *thin-film preparation.* Single-crystal Cu(100) films, ~500 Å thick, were grown on

*These authors contributed equally to this work.
†Contact author: gzhou@binghamton.edu

NaCl(100) substrates by electron-beam evaporation. Similarly, Cu-15 at.% Au(100) single-crystal thin films with ∼500 Å thickness were grown on NaCl(100) by *e*-beam coevaporation of Cu and Au, where the alloy composition was controlled by adjusting the evaporation rate of the two electron guns. Following deposition, the NaCl substrate was dissolved in de-ionized water, which yielded freestanding Cu and $Cu_{85}Au_{15}$ films that were subsequently transferred onto a TEM grid. These freestanding films underwent annealing in H_2 inside the environmental TEM, resulting in the formation of holes and tears with faceted edges. This process is akin to the mechanical cleavage of crystals in a vacuum environment. The freshly generated facets from the H_2 annealing process are atomically clean and provide an ideal substrate for conducting cross-sectional TEM observations. This approach allows us to study O adsorption induced structural changes that occur in the surface and subsurface regions when switching from the H_2 to an O_2 atmosphere.

In situ environmental TEM imaging. Our *in situ* TEM experiments were conducted using a dedicated environmental TEM (FEI Titan 80-300) equipped with an objective-lens aberration corrector and differential pumping system. The Cu and $Cu_{90}Au_{10}$ films were first annealed inside the TEM at ∼350 °C in H_2 at a gas pressure of ∼0.001 Torr. This annealing process served the dual purpose of removing any native oxide present on the films and inducing the formation of faceted holes. The successful elimination of the native oxide layer and the attainment of a clean surface were verified through high-resolution transmission electron microscopy (HRTEM) imaging, electron diffraction, and electron energy-loss spectroscopy (EELS) measurements, ensuring that the thin films annealed in the H_2 gas flow were free from oxide contamination.

Subsequently, the cleaned samples were exposed to a flow of O_2 gas to initiate the oxidation process. *In situ* HRTEM imaging of the oxidation process was captured using a camera capable of recording at 25 frames per second. Notably, the *in situ* HRTEM imaging experiments were performed with thin-film specimens at elevated temperature and in gas flow, where significant atom mobility and specimen drift induced by thermal and gas injection can affect detrimentally the image contrast and resolution that can be achieved in practice.

Density-functional theory (DFT) calculations. All calculations were performed using DFT implemented in the Vienna *Ab initio* Simulation Package (VASP) codes. In these calculations, the valence electron states were expanded using a plane-wave basis set with an energy cutoff 400 eV [16–19]. Exchange and correlation were treated within the generalized gradient approximation (GGA), using the Perdew-Burke-Ernzerhof (PBE) functional [20,21]. Given the strong correlation effects among the partially filled Cu 3*d* electrons, the Hubbard parameter, *U*, was introduced for the Cu 3*d* electrons to account for the on-site Coulomb interaction, based on the well-established GGA+*U* method. According to previous studies, the values of 6 and 0 eV were adopted for the two Coulombic parameters *U* and *J*, respectively [22]. However, it is noteworthy that our results from both GGA and GGA+*U* methods show similar outcomes. This consistency suggests that the Hubbard *U* correction may not exert a significant influence on the results for the present Cu_2O/Cu system, largely due to the ultrathin nature of the Cu_2O overlayer [only one atomic layer thick on the Cu(110) substrate]. For the Cu_2O/Cu surface model, a (4×2×1) *k*-point grid within the Monkhorst-Pack scheme in the Brillouin zone was employed. We used the (10×9) interface configuration to model the Cu_2O/Cu interface structure. In this (10×9) model, we used periodically repeated six-layer slabs with the bottom two layers fixed. All our calculations were spin averaged, except for isolated molecular and atomic oxygen. The surface structures were fully relaxed using the conjugate gradient method until the forces on each atom were less than 0.015 eV/Å. We calculated the lattice parameter of Cu to be 3.64 Å, which is in good agreement with previous calculations and the experimental value of 3.61 Å [23,24].

We investigated the adsorption of O and Cu atoms to determine the evolution of the surface structure. The most stable configuration identified after adsorbing a Cu or O atom was used as the reference state for the next atom to be adsorbed. The adsorption energy E_{ads} was calculated using the equation $E_{ads} = E^{tot}_{slab} - E_{Cu} - E_{atom}$, where E^{tot}_{slab} is the total energy of the whole system with the adsorbed atom, E_{Cu} is the free energy of the slab without the adsorbed atom, and E_{atom} is the energy of the adsorbed atom. For atomic O, E_{atom} equals half of the energy of an isolated O_2 molecule, and for Cu, E_{atom} is the energy of the Cu atom in the bulk. Meanwhile, the nudged elastic band (NEB) method was employed to model the diffusion pathway and associated energy barriers. At least five intermediate images were added between the initial and final states. All the atomic structures were visualized using the Visualization for Electronic and Structure Analysis (VESTA) program.

III. RESULTS AND DISCUSSION

Our oxidation experiments are performed in a dedicated ETEM equipped with a differential pumping system and a gas injection system for introducing gas flow into the sample region. *In situ* TEM imaging of the oxidation process is carried out in a cross-sectional view along the Cu(110) and $Cu_{85}Au_{15}$(110) facets, which are created *in situ* by annealing the films at 350 °C in H_2 to generate cracks and tears with faceted edges that are oxide free (Supplemental Fig. 1 in the Supplemental Material [25]). This process mimics crystal cleavage in vacuum, where the freshly created surface facets are oxide free and ideal for cross-sectional TEM observations of oxidation-induced structural changes in the surface and subsurface regions.

Among the low-index Cu surfaces, the O/Cu(110) is particularly intriguing because the O adsorption results in two distinct reconstructions preceding the bulk oxide formation. Initially, upon exposure to O_2, Cu(110) undergoes a transformation to the added-row (2×1)-O reconstruction (Supplemental Fig. 2 and Supplemental *in situ* TEM Movie 1 [25]). This structure is characterized by the formation of Cu-O-Cu chains along the [001] direction, occurring in every other $[1\bar{1}0] - (1\times1)$ lattice spacing, with an O coverage of 1/2 monolayer (ML) [26–29]. With further O_2 exposure, it transitions to the $c(6\times2)$-O reconstruction (Supplemental Fig. 3 and Supplemental *in situ* TEM Movie 2 [25]). The latter reconstruction comprises two adjacent [001]-oriented Cu-O-Cu

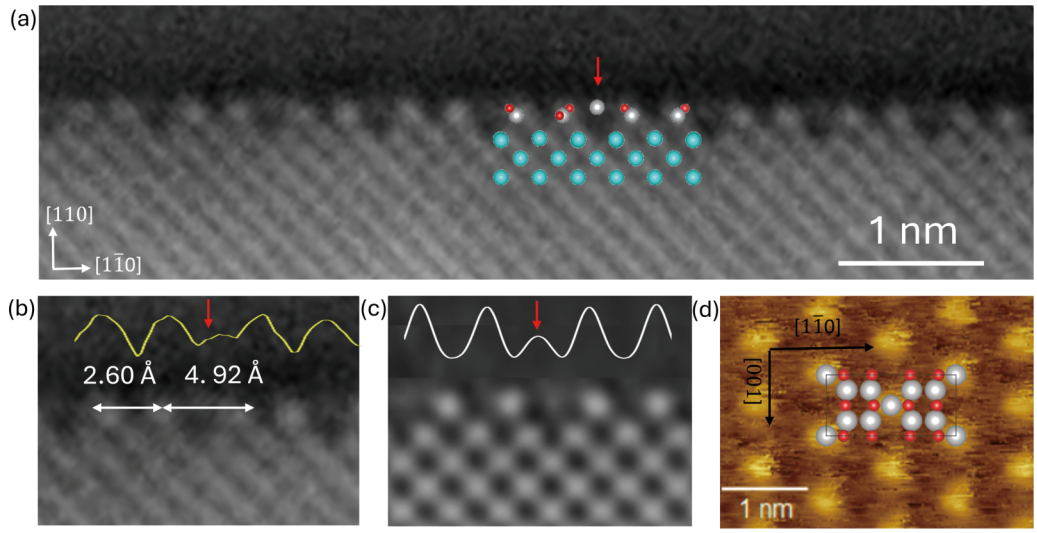

FIG. 1. HRTEM image of the $c(6\times2)$-O reconstruction of Cu(110) at 350 °C and 7.5×10^{-6} Torr O_2. (a) Cu(110)-$c(6\times2)$-O reconstruction. Inset: Side view of the DFT-relaxed $c(6\times2)$-O structure model overlaid onto the HRTEM image. (b), (c) Magnified views of the HRTEM image in (a) and corresponding simulated HRTEM image. Inset: Intensity profile along the topmost atomic layer. (d) Topographic STM image of the $c(6\times2)$-O formed on Cu(110) at 350 °C and 1×10^{-5} Torr O_2. Inset: Top view of the DFT-relaxed Cu(110)-$c(6\times2)$-O reconstruction overlaid onto the STM image. Cyan, gray, and red balls represent substrate Cu, Cu in $c(6\times2)$-O, and O atoms, respectively. The red arrows in (a)–(c) correspond to the isolated Cu columns within the $c(6\times2)$-O structure.

chains in every three [1$\bar{1}$0]-(1×1) lattice spacings with a saturated O coverage of $\theta = 2/3$ ML [27,30–37].

Figure 1(a) shows a high-resolution (HR) TEM image of the Cu(110) surface, observed along the [001] zone axis, following exposure to $p\ O_2 = 7.5\times10^{-6}$ Torr at 350 °C. The arrangement of atom columns in the topmost surface layer differs from that in the bulk, displaying two consecutive bright atom columns and a faintly visible atom column within every three [1$\bar{1}$0]-(1×1) lattice spacings in the topmost layer. Figure 1(b) depicts a magnified view of the HRTEM image and image intensity profile taken along the topmost layer, revealing a spacing of ∼2.6 Å between the two adjacent bright atom columns and a spacing ∼4.92 Å between two bright atom columns with a noticeably dim atom column situated between them.

For the $c(6\times2)$-O reconstruction, the terms "6" and "2" denote 6 times and 2 times the lattice spacings along the [1$\bar{1}$0] and [001] directions of the Cu(110) substrate, respectively. The former can be directly determined from the HRTEM images, as shown in Fig. 1(a). However, discerning the latter directly from the HRTEM imaging along the [001] projection view is not feasible. Therefore, distinguishing the periodicity along the [001] direction based solely on the [001]-projected HRTEM images is not possible.

To illustrate the atomic structure observed in the HRTEM image more clearly, we conducted scanning tunneling microscopy (STM) imaging on a single-crystal Cu(110) surface under O_2 dosing conditions similar to those used in the *in situ* HRTEM experiments. Figure 1(d) shows a representative topographic STM image of the $c(6\times2)$-O structure, where it is evident that the isolated Cu atoms in the $c(6\times2)$-O reconstruction protrude approximately 0.69 Å higher than the adjacent Cu-O-Cu chains. Consequently, the bright protrusions in the STM image correspond to these isolated Cu atoms, while the Cu-O-Cu chains are not visible. The STM image clearly reveals the periodicities of the $c(6\times2)$-O structure along both the [1$\bar{1}$0] and [001] directions of the Cu(110) substrate, demonstrating 6 times the lattice spacing along the [1$\bar{1}$0] direction and 2 times the lattice spacing along the perpendicular [001] direction. This structural detail is further elucidated by overlaying the DFT-relaxed $c(6\times2)$-O structure model onto the STM image, providing a visual representation of the precise surface atomic arrangement.

Figure 1(c) presents a simulated HRTEM image (Supplemental Fig. 4 [25]) based on the DFT-optimized Cu(110)-$c(6\times2)$-O structure model shown in Fig. 1(d). The simulated image closely resembles the experimental HRTEM image in Fig. 1(b), including both the bright and notably dimmed atom columns. As illustrated by the overlaid side view of the $c(6\times2)$-O structure in Fig. 1(a), the measured spacings match the $c(6\times2)$-O reconstruction. Here, the bright atom columns represent the [001]-oriented Cu-O-Cu chains, while the faintly visible atom columns correspond to the [001] rows containing isolated Cu atoms. This correspondence is further confirmed by the analysis of the image intensity profile, indicating that the intensity of the isolated Cu columns is ≈70% weaker than that of the Cu-O-Cu columns in both the experimental and simulated HRTEM images [Figs. 1(b) and 1(c)].

Figure 2(a) illustrates a HRTEM image of the Cu(110) after further exposure of the Cu(110)-$c(6\times2)$-O to $p\ O_2 = 7.5\times10^{-6}$ Torr at 350 °C, revealing the formation of a monolayer-thick oxide layer. The measured lattice spacing (∼2.82 Å) in the oxide overlayer matches that of the Cu_2O structure. The Cu_2O monolayer shows a slightly wavy undulation with hills and valleys parallel to the [001] direction of the Cu(110) surface. As measured from the HRTEM image in Fig. 2(a), the undulated Cu_2O overlayer has a peak to

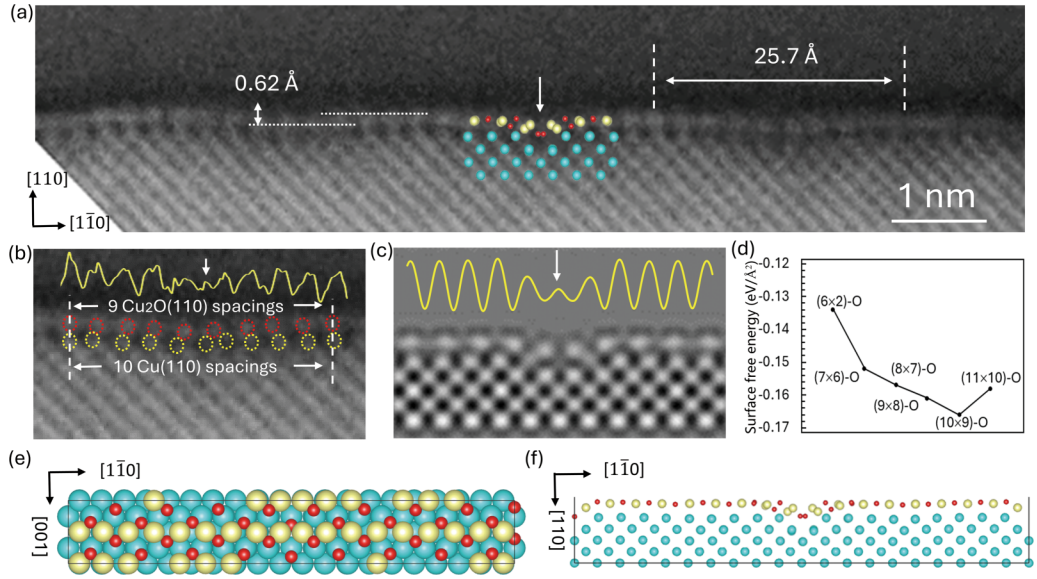

FIG. 2. HRTEM image of monolayer-thick Cu_2O on Cu(110) formed at 350 °C and 7.5×10^{-6} Torr O_2. (a) Monolayer-thick Cu_2O with the (10×9) interface matching with the Cu(110) substrate. Inset: Side view of the monolayer Cu_2O structure overlaid onto the HRTEM image. (b) Magnified view of the HRTEM image in (a). Inset: Intensity profile along the interfacial Cu layer marked by the dotted yellow circles. (c) Corresponding simulated HRTEM image and intensity profile along the interfacial Cu layer marked by the dashed white line. (d) DFT-computed surface free energies for various interfacial configurations between a monolayer of Cu_2O and the Cu(110) substrate, compared with the $c(6\times2)$-O surface reconstruction. (e), (f) Top and side views of the DFT-relaxed structure of monolayer Cu_2O on Cu(110). Cyan, yellow, and red balls represent substrate Cu, Cu in Cu_2O, and O, respectively. The white arrows in (a)–(c) indicate the vacant Cu column of the Cu substrate along the downward relaxation of the O atoms in the Cu_2O overlayer.

valley height of ∼0.62 Å and a peak to peak spacing of ∼25.7 Å. This undulation wavelength is equivalent to the (10×9) interface matching, in which ten Cu spacings in the Cu substrate match nine Cu spacings in the Cu_2O overlayer, as marked by the yellow and red dashed circles in an enlarged view of the HRTEM image [Fig. 2(b)]. Notably, while the (7×6) interface would result in the minimum lattice mismatch strain (1.22%) for the lattice constants of bulk Cu_2O (4.269 Å) and Cu (3.61 Å), the ultrathin nature of the Cu_2O overlayer significantly reduces its rigidity, allowing the interfacial atoms to adjust their positions into the (10×9) interface, which is closer to the (1×1) coherent interface matching than the (7×6) interface.

The preference for the (10×9) interface matching is further supported by our DFT-computed surface free energies for various interfacial configurations between a monolayer of Cu_2O and the Cu(110) substrate, including (7×6), (8×7), (9×8), (10×9), and (11×10), as well as the $c(6\times2)$-O surface reconstruction. As shown in Fig. 2(d), our DFT results indicate that the $c(6\times2)$-O surface reconstruction exhibits the highest surface energy, suggesting a tendency to oxidize into a monolayer of Cu_2O. Among the various interfacial configurations, the (10×9) interface displays the lowest surface energy, indicating its stability as the most favorable configuration. Therefore, we adopt the (10×9) interface structure for subsequent DFT modeling.

Figure 2(b) also presents the image intensity profile taken along the interfacial Cu layer marked by the yellow dotted circle. It reveals that the valley region has a weaker image contrast of the Cu lattice. Similar to the weakened image contrast from the isolated Cu chains (containing vacancies) in the $c(6\times2)$-O surface layer [Fig. 1(a)], the reduced image intensity of the Cu atom columns in the valley region suggests the presence of atomic vacancies to induce the grooving of the oxide film. Based on the above analysis of the HRTEM image, we therefore construct a structure model containing a monolayer Cu_2O film with the (10×9) interfacial matching with the Cu(110) substrate and aggregated atomic vacancies within the three [001] columns (one in the middle with 100% vacancies, and the two adjacent ones with 50% vacancies) in the topmost plane of the Cu(110) substrate, and then use DFT to obtain the minimum-energy structure [Figs. 2(e) and 2(f)]. It is worth mentioning that the (10×9) supercell was doubled to (20×18) for our DFT calculations. This adjustment was necessary because the Cu_2O structure contains two distinct types of O positions. By employing the (20×18) cell, we satisfy the periodic structure requirements and can examine both types of O sites within the same cell.

As illustrated by the overlaid side view of the DFT-optimized structure model in Fig. 2(a), the lattice O atoms directly above the completely vacant column fall into the vacant sites, and the adjacent Cu atoms in the Cu_2O overlayer also experience downward relaxation toward the two substrate Cu columns containing 50% Cu vacancies. This downward relaxation of the Cu and O atoms in the Cu_2O overlayer above the aggregated Cu vacancies of the Cu substrate leads to the local grooving of the oxide film. This is further corroborated by HRTEM image simulations (Supplemental Fig. 5 [25]) based on the DFT-optimized structure model [Fig. 2(d)]. As depicted in Figs. 2(b) and 2(c), the simulated HRTEM image closely aligns with the experimental HRTEM image, including the grooving morphology of the Cu_2O overlayer

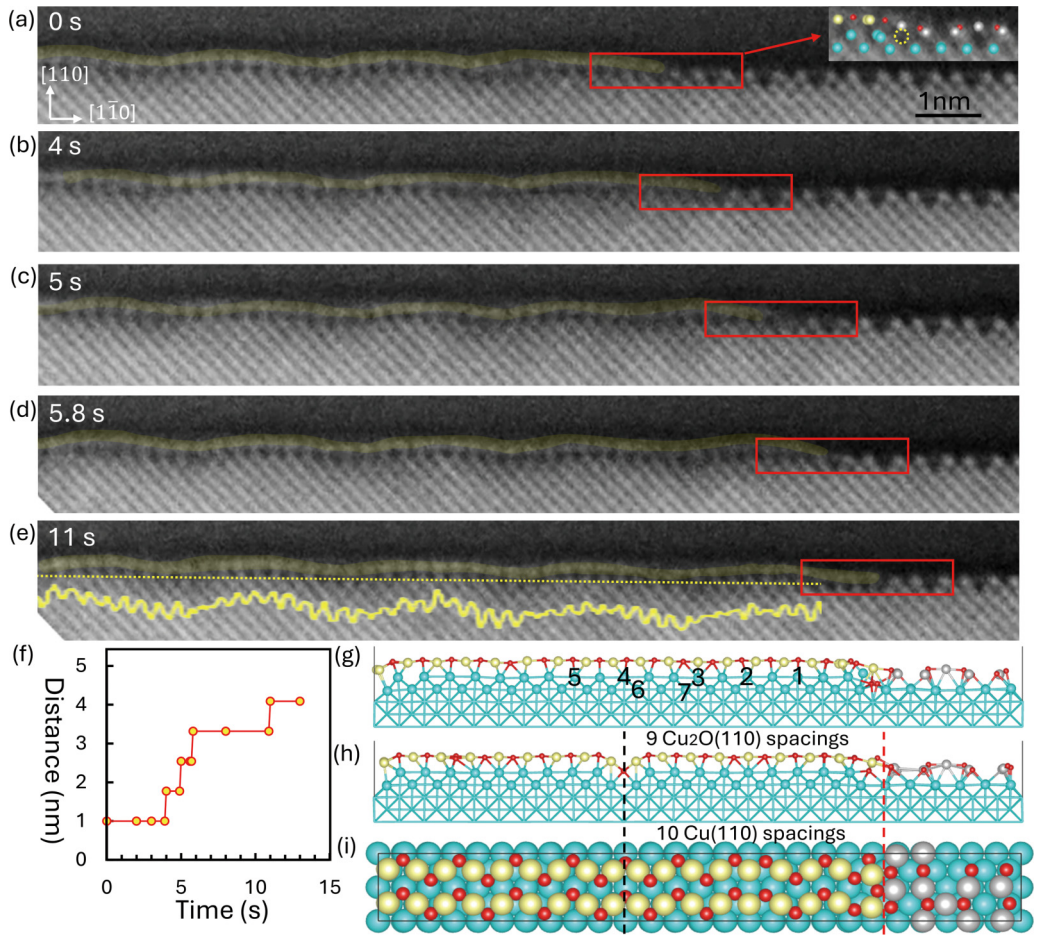

FIG. 3. *In situ* atomic-scale imaging of the intermittent $c(6\times2)$-O → Cu_2O transformation while exposing Cu(110) at 350 °C to 7.5×10^{-6} Torr of O_2 gas flow. (a)–(e) Time-sequence HRTEM images (Supplemental *in situ* TEM Movie 3 [25]) revealing the stop-and-go step flow of monolayer-thick Cu_2O, where the Cu_2O growth front is repeatedly pinned for about 1–4 s at the isolated Cu columns of the $c(6\times2)$-O terrace. Upper-right insets: Zoomed-in view and overlaid atomic structure of the Cu_2O growth front; the yellow dashed circles represent the Cu vacancy underneath the isolated Cu column in the $c(6\times2)$-O reconstruction. Bottom inset in (e): Intensity profile along the yellow dashed line. Pseudo color is applied to the Cu_2O layer for visual clarity. (f) Distance-time plot measured from Supplemental Movie 3 [25], showing the stop-and-go flow of the growth front of the Cu_2O layer. (g) Modeling the injection of vacancies generated at the $c(6\times2)$-O → Cu_2O transformation front into possible lattice sites labeled as 1–7. (h), (i) Side and top views of the DFT-relaxed structure, showing downward relaxation of the Cu and O atoms in the monolayer Cu_2O above the injected Cu vacancy column. The dashed black and red lines mark the Cu_2O growth front for O adsorption induced vacancy injection and the energetically preferred location for the aggregation of the injected vacancies, respectively. Cyan, yellow, gray, and red balls represent substrate Cu, Cu in Cu_2O, Cu in $c(6\times2)$-O, and O, respectively.

and the weakened image intensity of the Cu substrate lattice underneath the valley region. It is worth noting that the wavy feature of the Cu_2O layer in the simulated HRTEM image appears less pronounced compared to what is observed in the experimental HRTEM image. This difference may arise from vacancies present deeper within the subsurface layers than those considered in our current slab model, which only accounts for Cu vacancies in the second atomic layer. Unfortunately, incorporating additional vacancies into deeper atomic layers would necessitate using a thicker slab model. However, constructing such supercells poses significant computational challenges due to the substantial increase in the number of atoms involved.

Figure 3 presents *in situ* HRTEM imaging of monolayer Cu_2O growth by consuming the existing $c(6\times2)$-O reconstruction on Cu(110) (Supplemental *in situ* TEM Movie 3 [25]). The surface exhibits a step-terrace configuration with a monoatomic Cu_2O step separating two distinct terraces. The lower terrace on the right shows the well-developed $c(6\times2)$-O reconstruction, while the upper terrace on the left features a monolayer-thick Cu_2O overlayer marked in yellow. As indicated by the white arrows in Figs. 3(a)–3(e), the growth of the monolayer Cu_2O occurs through lateral movement of the monatomic Cu_2O step toward the $c(6\times2)$-O reconstructed terrace, resulting in the $c(6\times2)$-O → Cu_2O transformation. The *in situ* TEM observation reveals that this transformation proceeds intermittently, characterized by a stop-and-go manner, by which the lateral propagation of the monoatomic Cu_2O step is repeatedly stopped with short pauses ranging from 1 to 4 s. This is shown in the measured distance-time plot of the lateral propagation of the monatomic Cu_2O step [Fig. 3(f)]. The insets in Figs. 3(a)–3(e) provide zoomed-in HRTEM images with the overlaid atomic structure of the growth front of the monolayer Cu_2O

film, illustrating that the intermittent transformation from $c(6\times2)$-O to Cu_2O is regulated by isolated Cu atom columns within the $c(6\times2)$-O reconstruction. Specifically, step-flow growth of the Cu_2O overlayer is momentarily halted at the isolated Cu atom column [Fig. 3(a)], before resuming its lateral propagation to the next isolated Cu atom column [Fig. 3(b)]. Upon this propagation, the two bright atom columns (Cu-O-Cu chains) and the dim atom column (isolated Cu column), corresponding to half the unit cell length of the $c(6\times2)$-O reconstruction, are converted into the monolayer-thick Cu_2O. This process of short pauses at isolated Cu columns followed by propagation by a half-unit-cell distance of the $c(6\times2)$-O reconstruction repeats, leading to the stop-and-go migration of the Cu_2O growth front toward the $c(6\times2)$-O region.

The intermittent $c(6\times2)$-O $\rightarrow$ Cu_2O transformation results in the formation of the monolayer Cu_2O on the unreconstructed (110) terrace of the Cu substrate. This is evidenced by the intact and immobile $Cu_2O(110)/Cu(110)$ interface observed during the oxide growth, suggesting that the Cu_2O film growth observed here does not involve bulk diffusion of Cu and O atoms across the oxide layer. The Cu_2O overlayer shows the periodic undulation with the hill and valley morphology illustrated in Fig. 2(a). As indicated by the intensity profile taken along the interfacial Cu layer marked by the yellow dashed line in Fig. 3(e), the weaker image intensity of the Cu substrate lattice in the valley regions is attributed to the self-assembly of atomic vacancies. The DFT-optimized structure model of the Cu_2O growth front is superimposed onto the inset zoomed-in HRTEM images in Figs. 3(a)–3(e), illustrating that the isolated Cu in the $c(6\times2)$-O reconstruction bonds with the O in the Cu_2O overlayer. This bonding results in the upward relaxation of the isolated Cu and thereby generates a Cu vacancy [marked by the dashed yellow circles in the overlaid structure in Figs. 3(a)–3(e)] beneath the Cu_2O growth front. As shown later from our DFT modeling in Fig. 5, the $c(6\times2)$-O $\rightarrow$ Cu_2O transformation involves O adsorption at the Cu_2O growth front, inducing migration of adjacent substrate Cu atoms toward the Cu vacancy, thereby resulting in the injection of the Cu vacancy either into the Cu bulk or at the Cu_2O/Cu interface.

We therefore examine the relative stability of various atomic sites, including the Cu_2O/Cu interface and the Cu bulk, to determine the fate of the injected Cu vacancies. Figure 3(g) illustrates a structure model comprising a monolayer of Cu_2O on the left and the $c(6\times2)$-O reconstruction on the right of the Cu(110) substrate. Our DFT calculations reveal that the most energetically favorable site for O adsorption is at the boundary between the monolayer Cu_2O and the $c(6\times2)$-O, specifically at the growth front of the Cu_2O overlayer. Upon O adsorption at the boundary, the adjacent interfacial Cu atom undergoes a lateral shift toward the adsorbed O, resulting in the injection of a Cu vacancy into the Cu_2O/Cu interface (further details are in Fig. 5). The injected Cu vacancy tends to migrate further, and our DFT results indicate that the most favorable location for the Cu vacancy to settle is at the interfacial Cu site labeled as site 4 (Supplemental Table 1 [25]), positioned ten Cu atoms away from the Cu_2O growth front. Subsequent Cu vacancies generated at the Cu_2O growth front aggregate preferentially at site 4, forming a column of Cu vacancies. This aggregation induces a local downward relaxation of the Cu and O atoms within the Cu_2O overlayer above the vacancy column by $\sim$0.51 Å [Figs. 3(h) and 3(i)], closely aligning with the experimentally measured peak to valley height of $\sim$0.62 Å. Consequently, the Cu_2O overlayer exhibits undulations, where nine $Cu_2O(110)$ spacings correspond to ten Cu(110) spacings of the Cu substrate, as illustrated in Fig. 3(h). This structural adaptation results in the experimentally observed (10×9) lattice matching of the $Cu(110)/Cu_2O(110)$ interface, shown earlier in Figs. 2(b) and 2(e). Hence, the hill and valley undulation of the Cu_2O overlayer is induced by the interfacial self-assembly of injected Cu vacancies generated at the Cu_2O growth front. This interfacial self-assembly of the Cu vacancies is further supported by our nudged elastic band (NEB) calculations, revealing a lower energy barrier of $\sim$0.42 eV for the diffusion of Cu vacancies along the Cu_2O/Cu interface compared to their migration into the Cu bulk (Supplemental Fig. 6 [25]).

Figure 4 presents *in situ* TEM imaging (Supplemental *in situ* TEM Movie 4 [25]) of the thickening of the Cu_2O film due to continued O_2 exposure. In Fig. 4(a), a monolayer-thick Cu_2O layer has formed on the Cu(110) via the intermittent $c(6\times2)$-O $\rightarrow$ Cu_2O transformation process as described in Fig. 3. It is noteworthy that the monolayer Cu_2O film exhibits slight deviation from the well-defined (10×9) wavy undulation observed in Fig. 3, likely due to the injection of additional vacancies into the Cu_2O/Cu interface during the monolayer Cu_2O growth. As marked by the white arrow in Fig. 4(b), the growth front of a new oxide layer enters the field of view from the right side, leading to the formation of a bilayer oxide film via the lateral ledge flow of the upper Cu_2O layer. This growth process occurs because of the diffusion of Cu and O adatoms to the oxide growth front. The surface undulation of the inner Cu_2O layer does not noticeably affect the ledge growth of the upper Cu_2O layer. This is evident from the monotonic migration of the growth front, which can be located at any surface location of the inner Cu_2O layer, as indicated by the white arrows in Figs. 4(b)–4(g). The continuous ledge migration of the upper Cu_2O layer is also evidenced from the distance-time plot of the growth front in Fig. 4(h), showing a nearly linear increase in growth distance without experiencing obvious intermittence.

It is notable that the leading edge of the upper Cu_2O layer exhibits relatively weaker image contrast and a less resolved lattice feature compared to its rear region. This phenomenon can be attributed to the highly kinked ledge of the growth front, as illustrated schematically in the inset of Fig. 4(d). This contrast with the $c(6\times2)$-O $\rightarrow$ Cu_2O transformation (Fig. 3), where the pinning effect of the isolated Cu columns in the $c(6\times2)$-O results in a straight ledge of the growth front of the Cu_2O layer.

The intensity profile taken along the red dashed line in Fig. 4(g) reveals a peak to peak spacing of $\sim$26.1 Å for the undulated Cu_2O layer, which remains nearly constant during the growth of the upper Cu_2O layer. This consistency suggests that the step-flow growth of the upper oxide layer is governed by the surface diffusion of Cu and O adatoms and does not involve the mass transport across the inner Cu_2O layer with the immediate subsurface region of the Cu substrate. Such mass transport, if present, would alter the concentration

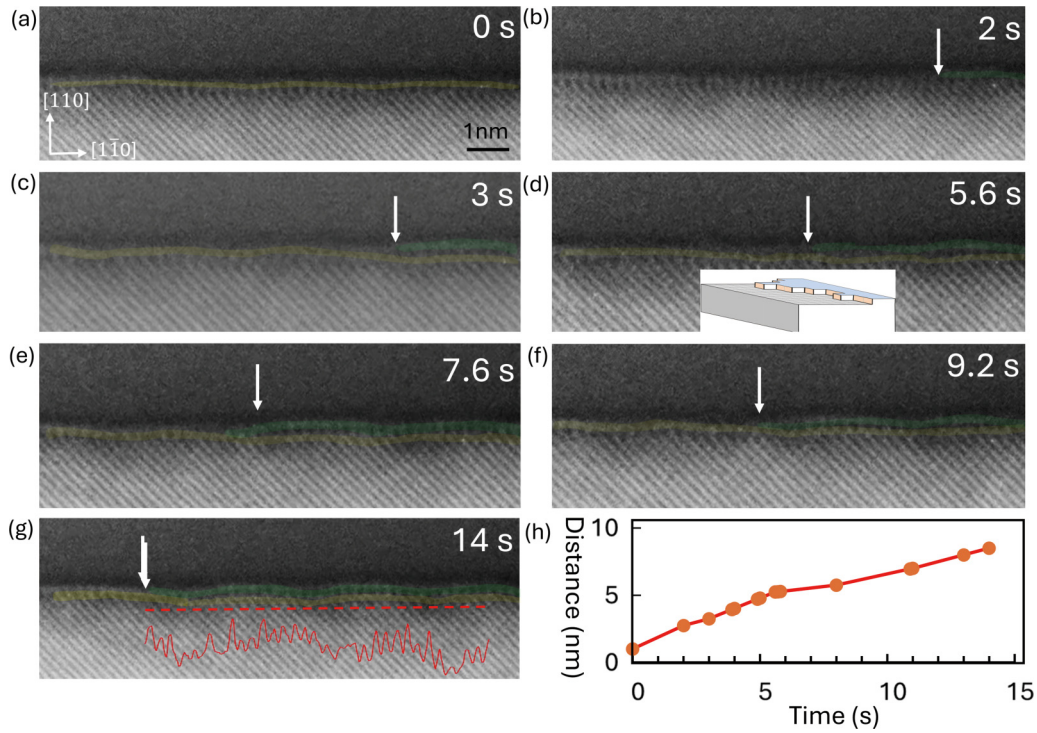

FIG. 4. *In situ* atomic-scale imaging of the formation of a bilayer oxide film on Cu(110) during oxidation at 350 °C and $\sim 7.5\times10^{-6}$ Torr O_2. (a)–(g) Time-sequence HRTEM images (Supplemental *in situ* TEM Movie 4 [25]) illustrating continuous step-flow growth of the upper monolayer-thick Cu_2O on the existing monolayer-thick Cu_2O. The inset in (d) illustrates the kinked ledge of the growth front. The inset in (g) is the intensity profile taken along the red dashed line. Pseudo yellow and green colors are applied to the inner and upper layers of Cu_2O, respectively, to guide the eye. (h) Distance-time plot measured from Supplemental *in situ* TEM Movie 4 [25].

and distribution of atomic vacancies in the Cu_2O/Cu interface region, leading to changes in the pattern of interfacial undulation.

The *in situ* TEM observations shown above reveal a key difference in the growth behavior between the two Cu_2O layers. Specifically, the inner Cu_2O layer grows via the stop-and-go propagation of the growth front, directly interacting with the $c(6\times2)$-O reconstruction. In contrast, the step flow of the upper Cu_2O layer propagates continuously. This difference can be attributed to the oxygen-induced surface restructuring, leading to periodic changes in the surface density of Cu and O atoms in the reconstruction region. The observed step flow of the Cu_2O growth front indicates an adatom process via the surface diffusion of O and Cu to the growth front (Supplemental Fig. 7 [25]), where O is supplied from dissociative adsorption of gaseous O_2 while Cu adatoms are sourced from low-coordinated surface sites of the Cu substrate (such as via step-edge detachment) and readily available at the elevated temperature. This adatom mechanism can be traced to the differing surface densities of Cu and O atoms between $c(6\times2)$-O and the monolayer Cu_2O. Specifically, the surface coverages of Cu and O for $c(6\times2)$-O are $\theta = 5/6$ and 2/3, respectively, corresponding to atomic surface densities of 0.09 and 0.07/Å^2. In contrast, for the monolayer (10×9) Cu_2O on Cu(110), both Cu and O surface densities are both 0.096/Å^2. Hence, in addition to the existing $c(6\times2)$-O, Cu_2O growth requires the incorporation of additional Cu and O from the surrounding area to the growth front.

The atomic mechanism behind the observed intermittent kinetics of the $c(6\times2)$-O $\rightarrow$ Cu_2O transformation is further elucidated through DFT modeling. Guided by the *in situ* TEM imaging in Fig. 3, Fig. 5(a) illustrates the DFT-optimized structure model of the heterophase boundary (Supplemental Fig. 8 [25]) formed between the leading edge of the (10×9) Cu_2O monolayer and the $c(6\times2)$-O reconstruction, where the Cu_2O growth front is anchored by the isolated Cu in the $c(6\times2)$-O. Since the surface oxidation is driven by the availability of O, we therefore first examine the possible surface sites for O adsorption, including the hollow sites and long bridge sites within the isolated Cu chain [marked as 1–3, respectively, in Fig. 5(a)]. According to our DFT calculations, the O adsorption at site 1 adjacent to the isolated Cu yields the most stable configuration, with a system energy drop of $\sim$0.92 eV. This induces the shift of the adjacent interfacial Cu atom [marked in blue in Fig. 5(b)], which then occupies the Cu vacancy and bonds with the newly adsorbed O at the growth front, thereby resulting in the injection of the Cu vacancy into the Cu_2O/Cu interface. After the first O adsorption, the hollow site [marked by the black dotted circle in Fig. 5(b)] within the isolated Cu chain becomes the most favorable site for the second O adsorption at the Cu_2O growth front. Figure 5(c) corresponds to the DFT-relaxed structure after the second O adsorption, from which we can identify that the Cu occupation at the interfacial Cu vacancy [marked by the red dotted circle in Fig. 5(c)] next to the growth front becomes the most favorable event. This process results in

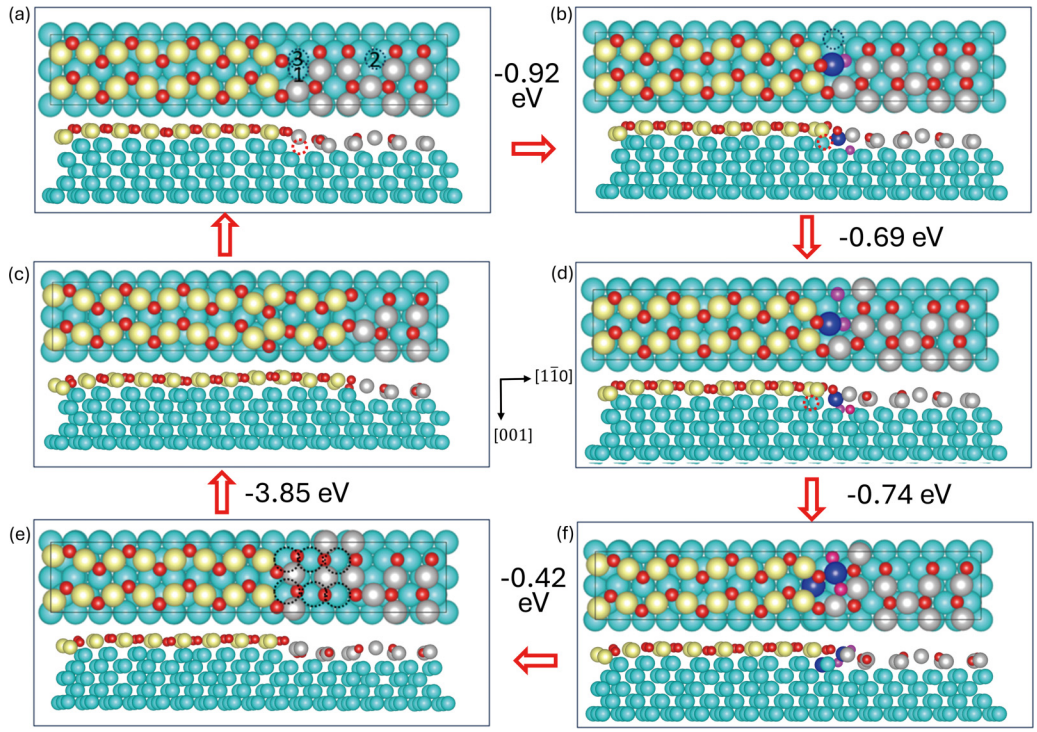

FIG. 5. DFT-obtained minimum-energy reaction pathway for the intermittent $c(6\times2)$-O $\rightarrow$ Cu_2O transformation, each with a half unit cell of the $c(6\times2)$-O. (a) Possible surface sites for O adsorption at the Cu_2O growth front pinned at isolated Cu of the $c(6\times2)$-O; the red dotted circle in the side view (lower panel) marks the Cu vacancy formed by the upward relaxation of the isolated Cu. (b) O adsorption (marked in purple) at the most favorable location of site 1 induces the upward relaxation of the substrate Cu atom (marked in blue) toward the adsorbed O. (c) Adsorption of the second O (marked in purple) at the most favorable hollow site. (d) Injection of the Cu vacancy [marked by the red dotted circle in the side view of (a)–(c)] to the most stable site of the Cu_2O/Cu interface [shown in Fig. 3(h)] results in the vacancy annihilation at the $c(6\times2)$-O $\rightarrow$ Cu_2O transformation front. (e) Adsorption of Cu adatoms at the hollow sites (marked by black dotted circles) of the $c(6\times2)$-O region. (f) Optimized structure model, showing the spontaneous transformation of the half unit cell of the $c(6\times2)$-O into the monolayer Cu_2O after adsorbing a total of two O adatoms, two substrate Cu atoms, and six Cu adatoms. Cyan, yellow, gray, and red balls represent substrate Cu, Cu in Cu_2O, Cu in $c(6\times2)$-O, and O, respectively.

the vacancy migration to the most stable interfacial site [as already shown in Fig. 3(h)], thereby causing the undulation of the Cu_2O film via the interfacial self-assembly of the injected vacancies.

Figure 5(d) illustrates the relaxed structure showing that the adsorption of two extra O atoms and one Cu atom from the reaction sequence shown in Figs. 5(a)–5(c) transforms the initially isolated Cu chain into the Cu-O-Cu chain with a system energy decrease of ~0.74 eV. Further structural optimization shows that this newly formed Cu-O-Cu chain tends to shift along the [001] direction, thereby resulting in its alignment with the adjacent Cu-O-Cu chains in the $c(6\times2)$-O with an additional drop in the system energy by ~0.42 eV, as shown in Fig. 5(e). At this point, the leading edge of the Cu_2O growth front reaches 1 monolayer (ML) of the O coverage without surface sites available for stable O adsorption. However, as marked by the black dashed circles in Fig. 5(e), the hollow sites within the Cu-O-Cu chain region are favorable for the adsorption of additional Cu adatoms. Figure 5(f) illustrates the DFT-relaxed structure after the Cu adsorption at these hollow sites, which shows the spontaneous upward relaxation of the O atoms in the original Cu-O-Cu chain to the half-tetrahedral sites at the surface, thereby resulting in the complete transformation of the three Cu-O-Cu chains in the $c(6\times2)$-O region into the monolayer Cu_2O. As a result, the leading edge of the Cu_2O growth front propagates to the next isolated Cu chain of the $c(6\times2)$-O [Fig. 5(f)], ready for another round of the Cu_2O growth by the half unit size of the $c(6\times2)$-O.

The pinning of the leading edge of the monolayer Cu_2O growth by the isolated Cu atom chains in the $c(6\times2)$-O is therefore attributed to the long-range diffusion of Cu and O adatoms required for transforming the isolated Cu and Cu-O-Cu chains in the $c(6\times2)$-O into the Cu_2O structure. As shown from the DFT modeling above, some of the Cu atoms are supplied from the immediate region of the Cu_2O/Cu interface, which results in the injection of the Cu vacancies generated at the growth front into the Cu_2O/Cu interface and leads to the hill and valley morphology of the Cu_2O film.

Finally, we demonstrate that the intermittent kinetics of the Cu_2O film growth also occurs during the surface oxidation of $Cu_{85}Au_{15}(110)$. Figure 6(a) illustrates the overall morphology of the $Cu_{85}Au_{15}(110)$ after its exposure to 1.35×10^{-4} Torr of O_2 gas and 350 °C, revealing the coexistence of $c(6\times2)$-O and Cu_2O in the topmost layer. The formation of the $c(6\times2)$-O reconstruction follows a similar pathway as the $c(2\times1)$-O $\rightarrow$ $c(6\times2)$-O transformation (Supplemental

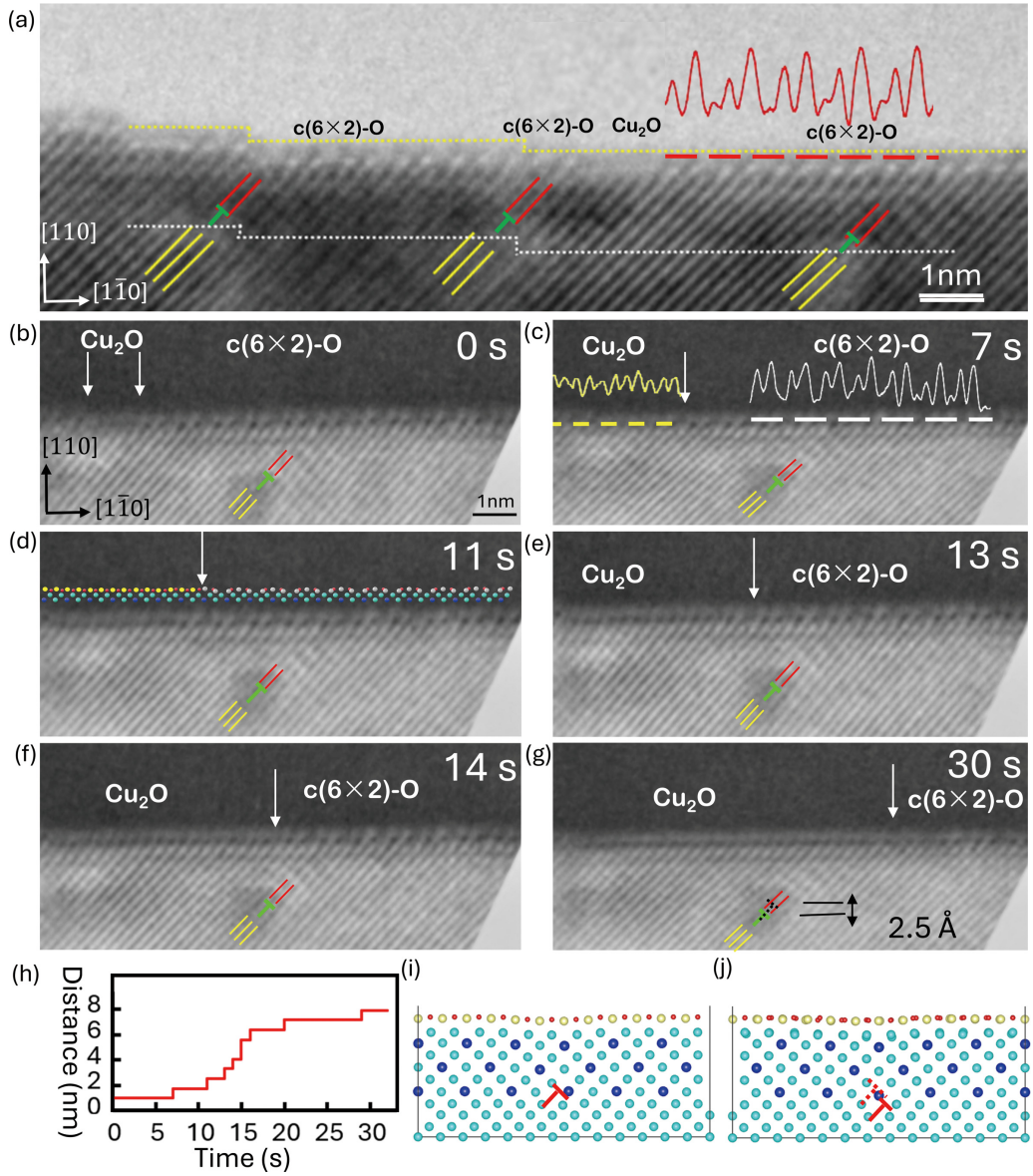

FIG. 6. *In situ* atomic-scale observation of the $c(6\times2) - O \rightarrow Cu_2O$ transformation on $Cu_{85}Au_{15}(110)$ at 350 °C and 1.35×10^{-4} Torr O_2. (a) Overall morphology of the $Cu_{85}Au_{15}$ (110) surface, featuring terraces separated by monoatomic steps, with coexisting $c(6\times2)$-O and Cu_2O regions at the topmost surface layer and an array of misfit dislocations at the interface between the Au-rich subsurface and the deeper Au-poor region. The top-right inset is the intensity profile of the $c(6\times2)$-O region along the dashed red line. (b)–(g) Time-sequence HRTEM images (Supplemental *in situ* TEM Movie 6 [25]) revealing the stop-and-go manner of the monolater Cu_2O growth by consuming the $c(6\times2)$-O reconstructed terrace. The insets in (c) are the intensity profiles of the (6×2)-O and Cu_2O regions, respectively. (h) Distance-time plot of the Cu_2O growth front measured from Supplemental Movie 6 [25]. (i), (j) DFT-optimized $Cu_2O(110)/Cu_{85}Au_{15}(110)$ structure models, depicting a misfit dislocation (marked by "T") at the interface between $L1_2$-ordered Cu_3Au in the subsurface and pure Cu in the deeper region, and the downward migration of the misfit dislocation after the vacancy injection into the dislocation core. Yellow and red balls represent Cu and O atoms in the monolayer Cu_2O, while green and blue balls correspond to Cu and Au atoms in the $Cu_{85}Au_{15}$ alloy, respectively.

Fig. 9 and Supplemental *in situ* TEM Movie 5 [25]). The $c(6\times2)$-O reconstruction is discernible by the intensity profile along the dashed red line, where the noticeably weaker peaks [marked by red arrows in the inset of Fig. 6(a)] correspond to the isolated Cu columns of the $c(6\times2)$-O, consistent with those observed in Fig. 1. Figure 6(a) also reveals the presence of an array of misfit dislocations in the subsurface region, ∼1.7 nm deep from the outermost surface layer. The formation of these misfit dislocations is induced by the Au enrichment in the subsurface, leading to an interface between the Au-rich and Au-poor bulk regions. As marked by the white and yellow dashed lines in Fig. 6(a), the misfit dislocations self-assemble into a stepped interface feature that correlates well with the stepped morphology of the surface. Correspondingly, all misfit dislocations maintain the same distance from the outermost surface layer.

Figures 6(b)–6(g) present *in situ* HRTEM images (Supplemental *in situ* TEM Movie 6 [25]) showing the intermittent kinetics of the Cu_2O film growth on the $Cu_{85}Au_{15}(110)$. In the beginning of the *in situ* image sequence, the surface is predominantly occupied by the $c(6\times2)$-O reconstruction. This is indicated by the intensity profile along the outermost surface layer, showing two consecutive bright atom columns and a faintly visible atom column within every three $[1\bar{1}0]-(1\times1)$ lattice spacings, consistent with Fig. 1. In contrast, the monolayer Cu_2O surface region shows uniform bright atom columns in the intensity profile [insets in Fig. 6(c)]. In Fig. 6(b), it is evident that the monolayer Cu_2O film and the $c(6\times2)$-O reconstruction are on the same terrace, with their boundary marked by the white arrow. As seen from Figs. 6(b)–6(g) and the distance-time plot in Fig. 6(h), the $c(6\times2)$-O $\rightarrow$ Cu_2O transformation occurs in the stop-and-go manner with the short pauses ranging from 1 to 9 s at the isolated Cu columns of the $c(6\times2)$-O. Each Cu_2O propagation event consumes half of the unit cell of the $c(6\times2)$-O region. Similar to the oxidation process observed in Cu(110)-$c(6\times2)$-O, this intermittent growth of the oxide film on $Cu_{85}Au_{15}(110)$ can be attributed to the long-range diffusion of additional Cu and O atoms required for the formation and conversion of the isolated Cu and Cu-O-Cu chains into the Cu_2O film.

However, the monolayer Cu_2O film on the $Cu_{85}Au_{15}(110)$ remains atomically flat without displaying any obvious hill and valley undulation. This disparity from the behavior on Cu(110) can be attributed to the presence of the misfit dislocations at the interface between the Au-rich and Au-poor bulk regions. As seen from Figs. 6(b)–6(g), the Cu_2O film exhibits a coherent (1×1) interface with the Au-rich subsurface region, which possesses a larger lattice constant than pure Cu. In contrast, the greater lattice mismatch between the Au-rich and Au-poor regions leads to the formation of misfit dislocations in the deeper region. The core of these misfit dislocations can act as a sink for the injection of atomic vacancies generated from the Cu_2O growth. This is corroborated by our *in situ* TEM imaging [Fig. 6(g)], which reveals a positive misfit dislocation climbing by 2 Cu(220) planes toward the Au-poor bulk region. Since misfit dislocations typically remain at the interface, it is reasonable to anticipate changes in the Au composition to accompany the interface shift and misfit dislocation climb in the local area.

This preference for segregation of injected vacancies to the misfit dislocation core is further supported by our DFT modeling. Figure 6(i) presents the DFT-optimized $Cu_2O(110)/Cu_{85}Au_{15}(110)$ structure model, in which $L1_2$-ordered Cu_3Au and pure Cu are used to represent the Au-rich region in the subsurface and the Au-poor region in the deeper region, respectively. The $Cu_2O(110)/Cu_3Au(110)$ interface exhibits a coherent (1×1) interface configuration, while the inner $Cu_3Au(110)/Cu(110)$ adopts a (13×12) interface matching with a misfit dislocation to accommodate the lattice mismatch ($\sim$3%). Our DFT calculations show that injecting atomic vacancies into the misfit dislocation core yields the lowest system energy (Supplemental Fig. 10 and Supplemental Table 2 [25]), accompanied by the relaxation of the misfit dislocation toward the Cu side [Figs. 6(i) and 6(j)]. As depicted in Fig. 6(i), the injection of vacancies into the misfit dislocation core does not induce obvious undulation in the monolayer Cu_2O film. This observation aligns with Figs. 6(a)–6(g), where the monolayer Cu_2O film remains atomically flat due to the considerable distance ($\sim$1.7 nm) between the misfit dislocations and the surface.

The results presented here highlight the crucial influence of oxygen-induced surface reconstruction on the kinetics of oxide film growth kinetics. Specifically, the transformation from $c(6\times2)$-O to Cu_2O is hindered by the presence of isolated Cu columns within the $c(6\times2)$-O reconstruction, which temporally pin the growth front. This pinning effect arises due to the nonlocal transport of Cu and O adatoms required for oxide formation. Our *in situ* TEM imaging also demonstrates that Cu vacancies, which are generated during oxide growth, preferentially migrate to the Cu_2O/Cu interface, leading to the formation of hill and valley undulations in the Cu_2O film. In these undulations, the valley regions correspond to nanocavities formed by the self-aggregation of injected atomic vacancies. In contrast, during $Cu_{85}Au_{15}(110)$ oxidation, atomic vacancies are directed toward interfaces between Au-rich and Au-poor regions deeper in the bulk, resulting in an atomically flat and adherent Cu_2O film.

The formation of oxide overlayers serves as a protective barrier against oxidation-induced degradation in metallic materials. However, the presence of cavities at the metal/oxide interface can compromise oxide adhesion, leading to oxide spallation under service conditions [38–42]. By comparing the oxidation behavior of Cu(110) and $Cu_{85}Au_{15}(110)$, we demonstrate the manipulability of the fate of the injected vacancies. Specifically, injected vacancies can be directed toward interfaces deep within the bulk of the alloy, thereby alleviating the metal/oxide interfacial cavitation issue and thus enhancing the adherence of the surface oxide layer. The well-established oxide breakdown model assumes that the interface between the scale and the metal undergoes a morphological evolution pathway, progressing from interfacial wrinkling to voiding, buckling, cracking, and ultimately spalling [43]. The results presented above provide atomistic insight into the microscopic origin of the interfacial wrinkling and voiding. Moreover, they highlight the potential to manipulate the morphological evolution pathway of the scale/metal, and thereby enhance the interfacial stability of the oxide scale, by engineering the composition and microstructure of the metals. This understanding opens up more avenues for designing more durable and reliable oxide-protected metallic systems.

IV. CONCLUSIONS

Using *in situ* environmental electron microscopy to monitor the surface oxidation of Cu(110) and $Cu_{85}Au_{15}(110)$, alongside atomistic modeling, we provide direct evidence of the intermittent kinetics of the oxide-film growth and oxide/metal interfacial undulation induced by reconstructive oxygen adsorption. These results demonstrate the critical role of the oxygen-induced surface restructuring in modulating the oxide film growth kinetics and the injection of atomic

vacancies into the Cu_2O/Cu interface, leading to the hill and valley undulation of the Cu_2O film. In contrast, we observe preferential injection of vacancies into the interfaces between Au-rich and Au-poor regions in the bulk during the oxidation of $Cu_{85}Au_{15}(110)$, resulting in an atomically flat and adherent Cu_2O film. These results offer mechanistic insights into the reaction pathway from oxygen-induced surface restructuring to subsequent bulk oxide formation and the manipulability of the fate of injected vacancies from oxide growth. The implications of these findings extend beyond the specific systems studied here, with relevance to various oxygen-metal systems and technological processes such as corrosion, heterogeneous catalysis, and thin-film processing.

ACKNOWLEDGMENTS

This work was supported by the U.S. Department of Energy, Office of Basic Energy Sciences, Division of Materials Sciences and Engineering under Award No. DE-SC0001135. This research used the resources of the Environmental TEM Catalysis Consortium (ECC), which is supported by the University of Pittsburgh and Hitachi High Technologies. Additionally, this research used the Theory and Computation resources of the Center for Functional Nanomaterials at Brookhaven National Laboratory, which is supported by the U.S. Department of Energy, Office of Basic Energy Sciences, under Contract No. DE-SC0012704.

[1] C. Gattinoni and A. Michaelides, Atomistic details of oxide surfaces and surface oxidation: The example of copper and its oxides, Surf. Sci. Rep. **70**, 424 (2015).

[2] G. Zhou, K. A. Unocic, C. Wang, Z. Shan, S. J. Haigh, and J. C. Yang, Revealing atomic-to-nanoscale oxidation mechanisms of metallic materials, MRS Bull. **48**, 852 (2023).

[3] D. J. Young, *High Temperature Oxidation and Corrosion of Metals* (Elsevier, Amsterdam, 2008).

[4] N. Birks, G. H. Meier, and F. S. Pettit, *Introduction to the High Temperature Oxidation of Metals* (Cambridge University Press, Cambridge, 2006).

[5] H. L. Xin, S. Alayoglu, R. Tao, A. Genc, C.-M. Wang, L. Kovarik, E. A. Stach, L.-W. Wang, M. Salmeron, G. A. Somorjai, and H. Zheng, Revealing the atomic restructuring of Pt–Co nanoparticles, Nano Lett. **14**, 3203 (2014).

[6] T. W. Hansen and J. B. Wagner, Catalysts under controlled atmospheres in the transmission electron microscope, ACS Catal. **4**, 1673 (2014).

[7] W. Yuan, Y. Wang, H. Li, H. Wu, Z. Zhang, A. Selloni, and C. Sun, Real-time observation of reconstruction dynamics on $TiO_2(001)$ surface under oxygen via an environmental transmission electron microscope, Nano Lett. **16**, 132 (2016).

[8] P. C. Vesborg, I. Chorkendorff, I. Knudsen, O. Balmes, J. Nerlov, A. M. Molenbroek, B. S. Clausen, and S. Helveg, Transient behavior of Cu/ZnO-based methanol synthesis catalysts, J. Catal. **262**, 65 (2009).

[9] W. Yuan, B. Zhu, K. Fang, X.-Y. Li, T. W. Hansen, Y. Ou, H. Yang, J. B. Wagner, Y. Gao, and Y. Wang, *In situ* manipulation of the active Au-TiO_2 interface with atomic precision during CO oxidation, Science **371**, 517 (2021).

[10] K. A. Unocic, D. Shin, R. R. Unocic, and L. F. Allard, NiAl oxidation reaction processes studied *in situ* using MEMS-based closed-cell gas reaction transmission electron microscopy, Oxid. Met. **88**, 495 (2017).

[11] A. A. Al-Ghamdi, M. Khedr, M. S. Ansari, P. Hasan, M. S. Abdel-Wahab, and A. Farghali, RF sputtered CuO thin films: Structural, optical and photo-catalytic behavior, Phys. E (Amsterdam) **81**, 83 (2016).

[12] P. Godowski, J. Onsgaard, A. Ga, M. Kondys, and Z. S. Li, Investigation of the CO+ NO reaction over the Cu (001) surface, Chem. Phys. Lett. **406**, 441 (2005).

[13] T. Tabakova, V. Idakiev, J. Papavasiliou, G. Avgouropoulos, and T. Ioannides, Effect of additives on the WGS activity of combustion synthesized CuO/CeO_2 catalysts, Catal. Commun. **8**, 101 (2007).

[14] J. A. Rodriguez, P. Liu, J. Hrbek, J. Evans, and M. Pérez, Water gas shift reaction on Cu and Au nanoparticles supported on $CeO_2(111)$ and ZnO(0001): Intrinsic activity and importance of support interactions, Angew. Chem. Int. Ed. **46**, 1329 (2007).

[15] Q. Jeangros, T. W. Hansen, J. B. Wagner, C. D. Damsgaard, R. E. Dunin-Borkowski, C. Hébert, J. Van Herle, and A. Hessler-Wyser, Reduction of nickel oxide particles by hydrogen studied in an environmental TEM, J. Mater. Sci. **48**, 2893 (2013).

[16] G. Kresse and J. Furthmüller, Efficient iterative schemes for *ab initio* total-energy calculations using a plane-wave basis set, Phys. Rev. B **54**, 11169 (1996).

[17] G. Kresse and J. Hafner, *Ab initio* molecular dynamics for liquid metals, Phys. Rev. B **47**, 558 (1993).

[18] G. Kresse and J. Hafner, *Ab initio* molecular-dynamics simulation of the liquid-metal–amorphous-semiconductor transition in germanium, Phys. Rev. B **49**, 14251 (1994).

[19] G. Kresse and J. Furthmüller, Efficiency of *ab-initio* total energy calculations for metals and semiconductors using a plane-wave basis set, Comput. Mater. Sci. **6**, 15 (1996).

[20] G. Kresse and D. Joubert, From ultrasoft pseudopotentials to the projector augmented-wave method, Phys. Rev. B **59**, 1758 (1999).

[21] J. P. Perdew, J. A. Chevary, S. H. Vosko, K. A. Jackson, M. R. Pederson, D. J. Singh, and C. Fiolhais, Atoms, molecules, solids, and surfaces: Applications of the generalized gradient approximation for exchange and correlation, Phys. Rev. B **46**, 6671 (1992).

[22] L. I. Bendavid and E. A. Carter, CO_2 adsorption on $Cu_2O(111)$: A DFT+U and DFT–D study, J. Phys. Chem. C **117**, 26048 (2013).

[23] D. Wu, J. Li, and G. Zhou, Oxygen adsorption at heterophase boundaries of the oxygenated Cu(110), Surf. Sci. **666**, 28 (2017).

[24] Y. Zhu, D. Wu, Q. Liu, J. T. Sadowski, and G. Zhou, Hydrogen-induced clustering of metal atoms in oxygenated metal surfaces, J. Phys. Chem. C **123**, 11662 (2019).

[25] See Supplemental Material at http://link.aps.org/supplemental/10.1103/PhysRevB.110.085402 for Supplemental Figs. S1–S10, Supplemental Tables S1 and S2, and Supplemental *in situ* TEM Movies 1–6 and corresponding captions.

[26] L. Li, N. Cai, W. A. Saidi, and G. Zhou, Role of oxygen in Cu (110) surface restructuring in the vicinity of step edges, Chem. Phys. Lett. **613**, 64 (2014).

[27] F. Jensen, F. Besenbacher, E. Lægsgaard, and I. Stensgaard, Surface reconstruction of Cu(110) induced by oxygen chemisorption, Phys. Rev. B **41**, 10233(R) (1990).

[28] H. Dürr, R. Schneider, and T. Fauster, Added-row growth of the (2×1)O-Cu(110) reconstruction, Phys. Rev. B **43**, 1802 (1991).

[29] J. Li, L. Li, and G. Zhou, The onset of sub-surface oxidation induced by defects in a chemisorbed oxygen layer, J. Chem. Phys. **142**, 084701 (2015).

[30] X. Duan, O. Warschkow, A. Soon, B. Delley, and C. Stampfl, Density functional study of oxygen on Cu(100) and Cu(110) surfaces, Phys. Rev. B **81**, 075430 (2010).

[31] D. Coulman, J. Wintterlin, R. Behm, and G. Ertl, Novel mechanism for the formation of chemisorption phases: The (2×1)O-Cu(110) "added row" reconstruction, Phys. Rev. Lett. **64**, 1761 (1990).

[32] S. Liem, G. Kresse, and J. Clarke, First principles calculation of oxygen adsorption and reconstruction of Cu (110) surface, Surf. Sci. **415**, 194 (1998).

[33] D. Wu, Y. Zhu, W. Shan, J. Wang, Q. Liu, and G. Zhou, Revealing an Intermediate Cu–O/OH superstructure on Cu (110), J. Phys. Chem. Lett. **13**, 2396 (2022).

[34] X. Lian, P. Xiao, R. Liu, and G. Henkelman, Communication: Calculations of the (2×1)-O reconstruction kinetics on Cu(110), J. Chem. Phys. **146**, 111101 (2017).

[35] L. Guillemot and K. Bobrov, Morphological instability of the Cu(110)–(2×1)-O surface under thermal annealing, Phys. Rev. B **83**, 075409 (2011).

[36] L. Li, Q. Liu, J. Li, W. A. Saidi, and G. Zhou, Kinetic barriers of the phase transition in the oxygen chemisorbed Cu(110)-(2×1)-O as a function of oxygen coverage, J. Phys. Chem. C **118**, 20858 (2014).

[37] Q. Liu, L. Li, N. Cai, W. A. Saidi, and G. Zhou, Oxygen chemisorption-induced surface phase transitions on Cu(110), Surf. Sci. **627**, 75 (2014).

[38] V. Maurice, G. Despert, S. Zanna, M.-P. Bacos, and P. Marcus, Self-assembling of atomic vacancies at an oxide/intermetallic alloy interface, Nat. Mater. **3**, 687 (2004).

[39] L. Rivoaland, V. Maurice, P. Josso, M.-P. Bacos, and P. Marcus, The effect of sulfur segregation on the adherence of the thermally-grown oxide on NiAl—II: The oxidation behavior at 900 °C of standard, desulfurized or sulfur-doped NiAl (001) single-crystals, Oxid. Met. **60**, 159 (2003).

[40] C. M. Wang, D. R. Baer, L. E. Thomas, J. E. Amonette, J. Antony, Y. Qiang, and G. Duscher, Void formation during early stages of passivation: Initial oxidation of iron nanoparticles at room temperature, J. Appl. Phys. **98**, 094308 (2005).

[41] D. Zimmermann, V. K. Tolpygo, M. Rühle, and D. R. Clarke, The role of oxidation-induced cavities on the failure of the thermally grown oxide on binary β-NiAl alloys, Int. J. Mater. Res. **94**, 157 (2003).

[42] H. Svensson, P. Knutsson, and K. Stiller, Formation and healing of voids at the metal–oxide interface in NiAl alloys, Oxid. Met. **71**, 143 (2009).

[43] Z. Suo, Wrinkling of the oxide scale on an aluminum-containing alloy at high temperatures, J. Mech. Phys. Solids **43**, 829 (1995).